

Data-efficient learning for 3D mirror symmetry detection

Yancong Lin, Silvia-Laura Pinteá, Jan van Gemert
Computer Vision Lab, Delft University of Technology, the Netherlands

Abstract

We introduce a geometry-inspired deep learning method for detecting 3D mirror plane from single-view images. We reduce the demand for massive training data by explicitly adding 3D mirror geometry into learning as an inductive prior. We extract semantic features, calculate intra-pixel correlations, and build a 3D correlation volume for each plane. The correlation volume indicates the extent to which the input resembles its mirrors at various depth, allowing us to identify the likelihood of the given plane being a mirror plane. Subsequently, we treat the correlation volumes as feature descriptors for sampled planes and map them to a unit hemisphere where the normal of sampled planes lies. Lastly, we design multi-stage spherical convolutions to identify the optimal mirror plane in a coarse-to-fine manner. Experiments on both synthetic and real-world datasets show the benefit of 3D mirror geometry in improving data efficiency and inference speed (up to 25 FPS).

1. Introduction

Symmetry exists in nature, in the man-made world, and in science and arts. Mirror symmetry, also known as bilateral or reflection symmetry, is an intrinsic property of many man-made objects, which allows us to infer the entire object from only partial observations, as demonstrated in the shape completion [5, 12] and single-view 3D reconstruction [23, 22, 21].

Front-facing objects often exhibit planar symmetry. However, most images in our daily life are not taken from the front-view and as a result, planar symmetry does not always exist in images due to the perspective effect. Thus, inferring 3D mirror symmetry has to handle perspective effects. Classic work on detecting single-view mirror symmetry relies on local feature matching and camera geometry reasoning [10]. This approach is able to predict mirror symmetry on textured images. However, for textureless objects and surfaces it is hard to find correspondences for feature matching.

Recently, deep learning-based approach outperforms classic work on detecting mirror symmetry by learning

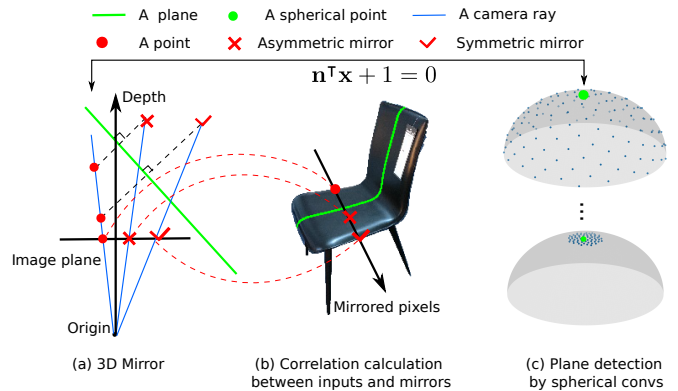


Figure 1: **3D mirror symmetry detection.** We identify 3D mirror plane by measuring the correlations between the input and its mirrors over depth. The mirrors are calculated by 3D mirror geometry (a), which localizes the reflections of a given pixel directly on the image plane (b). The 3D mirror is explicitly encoded without learning from data. We consider the correlations as a feature descriptor for each plane sampled on a hemisphere and adopt multi-stage spherical convolutions to localize the optimal plane hierarchically (c). We lay the ground truth symmetry axis (in green) on top of the image.

dense features from images [22, 25]. This compensates the disadvantage of unreliable local features and improves the overall performance of symmetry-dependent 3D reconstruction. However, this approach typically requires large annotated datasets, such as ShapeNet [2].

In this paper, we aim to detect 3D mirror symmetry from single-view images by using deep learning in a data-efficient manner. The symmetry task is to predict the normal direction of the mirror plane and we propose to explicitly incorporate into neural networks the knowledge of 3D mirror geometry such that the spatial reflection of pixels with regard to the plane no longer needs to be learned from data, as shown in Fig. 1. Moreover, the mirror geometry associates each plane with a unique point on a hemisphere, thus enabling the usage of spherical convolutions to identify the optimal plane from its neighbors. To further reduce the search space, we design multi-stage spherical convolutions

to hierarchically pinpoint the best prediction.

Our work takes the strengths of both the geometry-based and learning-based approaches. On one hand, we take the advantage of neural networks in learning powerful features from images. On the other hand, we manually incorporate 3D mirror geometry into learning, as neural networks lack the ability of such geometric operations by design.

This paper makes the following contributions: (1) we explicitly add 3D mirror geometry into neural networks for finding symmetric correspondences; (2) we design multi-stage spherical convolutions to detect a mirror plane in a coarse-to-fine manner; (3) We improve data efficiency of learning-based mirror symmetry detection, especially relevant for when training data is scarce; (4) we experimentally demonstrate the advantage of our approach in improving both performance and inference speed (approximately 25 frames per second).

2. Related work

Planar symmetry detection. The work in [11] presents a thorough overview of existing methods on 2D symmetry detection by organizing a series workshops. Further work in [3] expands the workshop by including other types of symmetries such as medial-axis-like symmetries and by adding synthetic 3D data. The work in [4] first adapts neural networks for planar symmetry detection and achieves competitive results. However, most objects in this challenge are strictly front-facing and therefore only exhibit planar symmetries. In addition, planar symmetry does not encode any 3D perspective information. Different from these works, we aim to detect 3D mirror symmetry from single-view images where images can be taken from any perspective.

3D mirror symmetry detection. 3D mirror symmetry is prevalent in both nature and the man-made world. There has been excellent research on utilizing geometric transforms for detecting mirror symmetries from 3D inputs [1, 16, 15]. The work in [1] detects mirror symmetry plane from point clouds via a 3D Hough Transform. The work in [15] relies on the Planar Reflective Symmetry Transform to find symmetry planes from 3D volumetric data. Similar to these works, we also make use of the 3D geometric knowledge for detecting mirror symmetries, but from single-view images only.

Recently, the work in [17, 5] take advantage of large datasets and employ neural networks for learning 3D symmetries. Despite being able to detect multiple symmetries, they rely on heavy post-processing procedures to find the optimal symmetry. Moreover, these models have only been tested on synthetic 3D datasets (i.e. ShapeNet [2] with voxelized volumes or RGB-D data). In contrast, we propose to learn 3D mirror symmetry in an end-to-end manner, and test on both synthetic and real-world 2D images.

3D mirror symmetry from single-view images. In [10], a two-stage approach is proposed to estimate mirror symmetry from 2D images. This approach first does correspondence matching and then applies RANSAC to identify the best symmetry plane. However, this strategy is no longer applicable in certain cases where textureless objects, smooth surfaces and repetitive patterns are present, because of lacking correspondences. Rather than relying on local feature matching, NeRD [25] makes use of neural networks to learn dense features and incorporates 3D mirror geometry into learning, making it the top-performing model. Inspired by NeRD, we also explicitly add geometric knowledge into learning. Different from NeRD which relies on large amounts of training data, we reduce the inference latency and the demand for massive data by calculating the correlations between the input and its mirrors and by introducing multi-stage spherical convolutions to the localize the optimal mirror plane.

3. Geometric priors for 3D mirror symmetry

Fig. 2 shows an overview of our model. Given an RGBA image as input, our model outputs the confidence all sampled planes being the mirror plane. We choose the plane with the highest confidence as our prediction. Although an object may admit multiple symmetries, we only predict the principal mirror symmetry, as in [25]. We explicitly add knowledge of 3D mirror geometry into deep networks to improve the data efficiency. There are three parts in our model: (1) feature extraction and correlation calculation, (2) 3D mirroring, (3) plane identification by spherical convolutions.

3.1. (i) Feature extraction and correlation calculation

We first learn semantic features from images via convolutional neural networks as in [25], resulting in a feature map \mathcal{F} of size $H \times W \times C$, where H , W , and C indicate height, width, and number of channels, respectively. Then, we calculate the intra-pixel correlation between each pair of points in the $H \times W$ grid by dot product over the channel dimension, resulting in a correlation tensor \mathcal{C} of size $H \times W \times H \times W$. \mathcal{C} indicates the extent to which a pixel resembles the others. A higher correlation implies higher visual similarity. We set H , W and C to 64.

3.2. (ii) 3D symmetries

Next, we feed the correlation tensor \mathcal{C} into the 3D mirror module which outputs a feature descriptor for each considered mirror plane. Given a randomly sampled plane, the 3D mirror module first computes the symmetric correspondences for each pixel at various depth, and then aggregates correlations between a pixel and its correspondences in a 3D correlation volume. The correlation volume indicates the

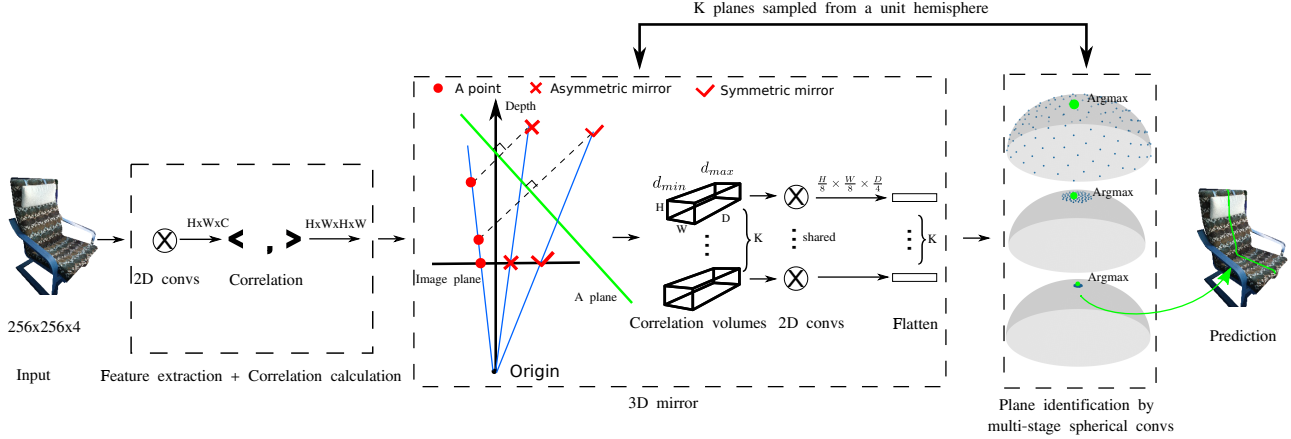


Figure 2: **Overview.** Our model includes three components: feature extraction and correlation calculation, 3D mirror and plane identification by spherical convolutions. We first calculate intra-pixel correlations using learned features. Then we build a correlation volume for each sampled plane, which is then flattened as a feature descriptor. We adopt spherical convolutions on uniformly sampled planes on a hemisphere to locate the optimal plane (highlighted in green).

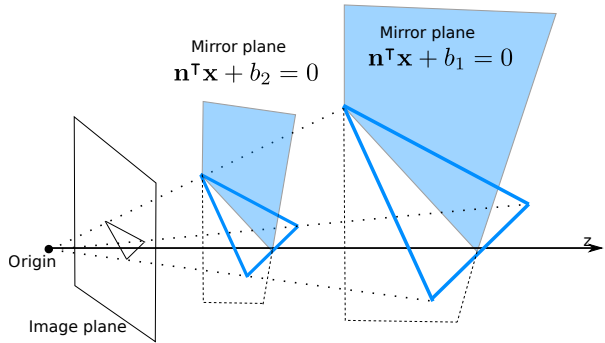


Figure 3: **Scale ambiguity.** The two objects (in blue) only differ in scale, but their projections on the image plane are the same. Therefore, we are unable to determine the scale of the object, or the actual value of the offset. In practice, we set $b = 1$.

resemblance between the input and its mirrors. A higher resemblance implies that the given plane is more likely to be the optimal mirror plane. The correlation volume is then downsampled and flattened into a 1D descriptor for the given plane. We define 3D mirror planes, elaborate correspondence calculation and describe 3D cost volumes as follows.

(ii.1) 3D mirror planes. A plane can be uniquely defined as $\mathbf{n}^T \mathbf{x} + b = 0$ by its normal direction $\mathbf{n} \in \mathbb{R}^3$ and offset $b \in \mathbb{R}$, where $\mathbf{x} \in \mathbb{R}^3$ represents points on the plane. However, we are unable to determine b due to the scale ambiguity [13, 25], as shown in Fig. 3. This is because one can move the scene arbitrarily along the normal direction \mathbf{n} and scale the scene accordingly without affecting the image. Therefore, the only variable to predict is the normal direction \mathbf{n} of the mirror plane. Moreover, given that a normal

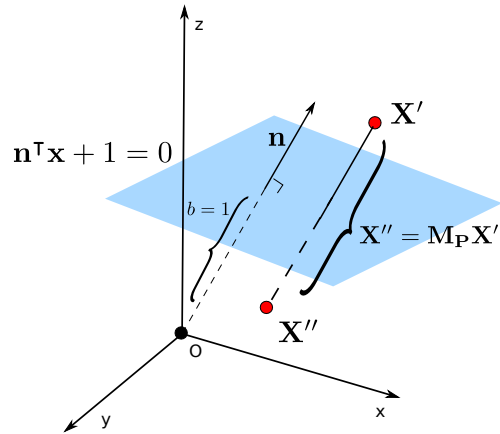


Figure 4: **3D mirror geometry.** 3D points \mathbf{X}' and \mathbf{X}'' are symmetric with respect to the given plane $\mathbf{n}^T \mathbf{x} + 1 = 0$. We represent $\mathbf{X}' \in \mathbb{R}^4$ and $\mathbf{X}'' \in \mathbb{R}^4$ in the homogeneous coordinate, where $\mathbf{X}'' = \mathbf{M}_P \mathbf{X}'$ as defined in Eq. (1). $\mathbf{M}_P \in \mathbb{R}^{4 \times 4}$ is the 3D mirror transformation uniquely determined by \mathbf{n} , allowing us to calculate mirrors explicitly [1, 10].

direction is equivalent to a point on a unit hemisphere, we can further define a plane as a spherical point. Thus we can sample planes from a unit hemisphere.

(ii.2) 3D mirror. Fig. 4 shows an illustration of 3D mirror geometry for a randomly sampled plane. The 3D mirror transformation $\mathbf{M}_P \in \mathbb{R}^{4 \times 4}$ associated to plane $\mathbf{n}^T \mathbf{x} + 1 = 0$ can be defined by Eq. (1), where $\mathbf{X}'' \in \mathbb{S}$ and $\mathbf{X}' \in \mathbb{S}$ are a pair of symmetric points and $\mathbb{S} \subset \mathbb{R}^4$ is the set of points on the object surface in the homogeneous coordinate [1, 10].

$$\mathbf{X}'' = \underbrace{\begin{pmatrix} \mathbf{I} - 2\mathbf{n}\mathbf{n}^\top & -2\mathbf{n} \\ \mathbf{0} & 1 \end{pmatrix}}_{\mathbf{M}_P} \mathbf{X}' \quad (1)$$

Given camera intrinsic matrix $\mathbf{K} \in \mathbb{R}^{4 \times 4}$, we can project both \mathbf{X}' and \mathbf{X}'' on the image plane by $\mathbf{x}' = \mathbf{K}\mathbf{X}'/d'$ and by $\mathbf{x}'' = \mathbf{K}\mathbf{X}''/d''$, where d' and d'' are the corresponding depth in the camera space. Therefore we can derive the constraint between projections \mathbf{x}' and \mathbf{x}'' as

$$\mathbf{x}''d'' = \mathbf{K}\mathbf{M}_P\mathbf{K}^{-1}\mathbf{x}'d' \quad (2)$$

where $\mathbf{x}' = [x', y', 1, 1/d']$ and $\mathbf{x}'' = [x'', y'', 1, 1/d'']$ indicate the coordinates of the projected points in the pixel space. Eq. (2) illustrates how to find the symmetric correspondence of a pixel at various depth, given a mirror plane.

(ii.3) 3D correlation volume. We follow Eq. (2) to localize the symmetric correspondences (x'', y'') for each pixel (x', y') at various depth $d \in \mathcal{D}$, where $\mathcal{D} = \{d_{min} + \frac{i}{D-1}(d_{max} - d_{min}) | i = 0, 1, \dots, D-1\}$. d_{min} and d_{max} are the minimal and maximal depth values. Subsequently, we index the correlation tensor at $\mathcal{C}(x', y', x'', y'')$ via bi-linear interpolation. Lastly, we fill in $\mathcal{V}(x', y', d)$ with the indexed value. We enumerate all $d \in \mathcal{D}$ for each pixel (x', y') in the $H \times W$ grid, thus obtaining a correlation volume \mathcal{V} of size $H \times W \times D$.

The correlation volume \mathcal{V} indicates the resemblance between the input and its mirrors at all sampled depth, thus facilitating deep networks to learn if there exists a visually similar reflection for the given plane. A higher similarity implies that the give plane is more likely to be a mirror plane. However, to identify the global mirror plane, we need to aggregate information over the entire \mathcal{V} . Otherwise, the model may only predict local symmetries. To this goal, we apply 2D convolutions to downscale \mathcal{V} , resulting in an output tensor of size $\frac{H}{8} \times \frac{W}{8} \times \frac{D}{4}$. The downscaled output is then flattened in to a 1D vector for further classification. By far, we are able to obtain a 1D feature descriptor for each plane sampled on the hemisphere.

3.3. (iii) Plane detection by spherical convolutions

To pinpoint the optimal mirror plane, we need an exhaustive search on the entire hemisphere, which is computationally infeasible. Instead, we adopt a multi-stage sampling strategy using Fibonacci lattice [6] in a coarse-to-fine manner. In practice, we sample planes for 3 stages to reach a desirable precision. $\mathbb{P}_i = \{\mathbf{n}^k\}_{k=1}^K \subset \mathbb{R}^3$ represents all sampled planes at i th stage, where \mathbf{n} is the normal direction, and K is the number of planes. This results in a spherical point cloud of size K at each stage, where each point (plane) is associated with an 1D feature descriptor. Since all K planes at each stage are uniformly sampled, we can utilize spherical convolutions to identify the most probable candidate by

comparing a plane with its neighbors. We use EdgeConv [20] to convolve at each stage. The EdgeConv module extracts features from a local neighborhood with a fully connected layer, a BatchNorm layer [8] and a LeakyReLU activation. We treat each sampled point as a node and compute the top 16 nearest neighbors for each node.

The multi-stage sampling differs in training and inference. During training, we uniformly sample K planes $\mathbb{P}_i = \{\mathbf{n}^k | \arccos(|\langle \mathbf{n}^k, \hat{\mathbf{n}} \rangle|) \leq \delta_i\}_{k=1}^K$ on the hemisphere at the i th stage and assign the nearest neighbor to the ground truth $\hat{\mathbf{n}}$ as the label. δ_i is the scale factor which defines the size of sampling region at the i th stage. We minimize the binary cross-entropy loss at each stage, averaged over the positive and negative samples respectively due to the class imbalance. During inference, we start with a uniform sampling of K planes $\mathbb{P}_1 = \{\mathbf{n}^k\}_{k=1}^K \subset \mathbb{R}^3$ on the whole hemisphere. Subsequently, we take from previous step the best prediction $\hat{\mathbf{n}}_{i-1}$ as the center and sample another K planes $\mathbb{P}_i = \{\mathbf{n}^k | \arccos(|\langle \mathbf{n}^k, \hat{\mathbf{n}}_{i-1} \rangle|) \leq \delta_i\}_{k=1}^K$. We choose the plane with the highest confidence as our prediction.

4. Experiments

4.1. Experimental setup

Datasets. We conduct experiments on ShapeNet [2] and Pixel3D [18]. The objects in both datasets are aligned in the canonical space such that the Y-Z plane is the 3D mirror symmetry plane. On the synthetic ShapeNet dataset, we use the same subset as in [25] for fair comparison. There are 175,122/500/8,756 images in the training/validation/test splits, respectively. All images are of size 256×256 pixels. On the real-world Pixel3d dataset, we also follow [25] to pre-process the data. We first crop the images to obtain the objects inside bounding boxes, Sequentially, we rescale them to 256×256 , and adjust the camera intrinsic matrix \mathbf{K} accordingly. This results in a dataset of 5,285 and 588 images for training and test respectively.

Evaluation. We follow [25] to evaluate all methods by measuring the angle difference of the plane normals between the ground-truth and predictions in the camera space. We calculate the percentage of the predictions that have a smaller angle difference than a given threshold and plot the angle accuracy (AA) curves.

Implementation details. We implement our model in Pytorch [14], and provide our code online. The $x = 0$ plane in the object space is considered as the ground truth because it is explicitly aligned for each object [2]. We set $d_{min} = 0.64$, $d_{max} = 1.23$ and $D = 64$ for depth. We do spherical convolutions at 3 scales and sample 128, 64, 64 symmetry planes at each scale. We set the scael factor to be $\delta = \{90.0^\circ, 12.86^\circ, 3.28^\circ\}$. All models are trained from scratch on each dataset on Nvidia RTX2080 GPUs with the

Adam optimizer [9], for 32 epochs at most. The learning rate and weight decay are set to be 3×10^{-4} and 1×10^{-7} . We decay the learning rate by 10 after 24 epochs. To maximize the GPU usage, we set batch size to 6. The inference speed is approximately 25 frames per second.

Baselines. We compare our model primarily with NeRD [25], the state-of-the-art work on 3D mirror symmetry detector, in all experiments. We also implement a simple baseline using direct regression to estimate the symmetry normal \mathbf{n} . We implement this baseline on top of a ResNet-50 [7] backbone with L1 loss. Front2Back [23] also detects 3D mirror symmetry using a variant of classical ICP approach. However, it requires depth map in advance and has only been tested on ShapeNet. RotCon [24] proposes a continuous representation for estimating 3D rotation. We use L1 loss for training and report its performance on both datasets. DISN [22] learns 6D rotation representation for estimating camera poses on ShapeNet. We recover the normal of the mirror plane from camera poses and report the performance of their pre-trained models on ShapeNet. NCOS [19] defines a *Normalized Object Coordinate Space (NOCS)* and identifies 6D representations of camera poses. We use NOCS to estimate the orientation of objects and show its result on ShapeNet.

4.2. Exp 1: Data efficiency

We first evaluate data efficiency by reducing the number of training samples to $\{50\%, 25\%, 10\%, 5\%, 2.5\%, 1\%\}$ on the ShapeNet dataset, which has approximately 200K training images in total. We train all models from scratch and compare the AA scores at 3° and 5° on the test set. We compare our model with NeRD which holds state-of-the-art result, as shown in Fig. 5. The two models have similar amount of parameters, thus removing the impact of parameters. In general, our model shows superiority over NeRD with the decrease of training samples, and the advantage accentuates on subsets with fewer than 10K images. In the 100% – 10% zone, we only observe marginal difference, while in the 10% – 1% zone, we witness a dramatic difference (up to 10%), indicating our model is more efficient in learning from limited data. Notably, our model is able to achieve similar results as NeRD with only half of the training data as indicated on the 2.5% and 5% subsets, thus verifying the superiority of our model in data efficiency.

4.3. Exp 2: Comparison with state-of-the art

4.3.1 Exp 2.1: Comparison on synthetic data

Fig. 6 and Tab. 1 shows the comparison among state-of-the-art models on the synthetic ShapeNet dataset. Our model shows competitive results and enjoys a considerable advantage in the low-error region. For example, the prediction error of our model is less than 1° in 80% test cases. NeRD

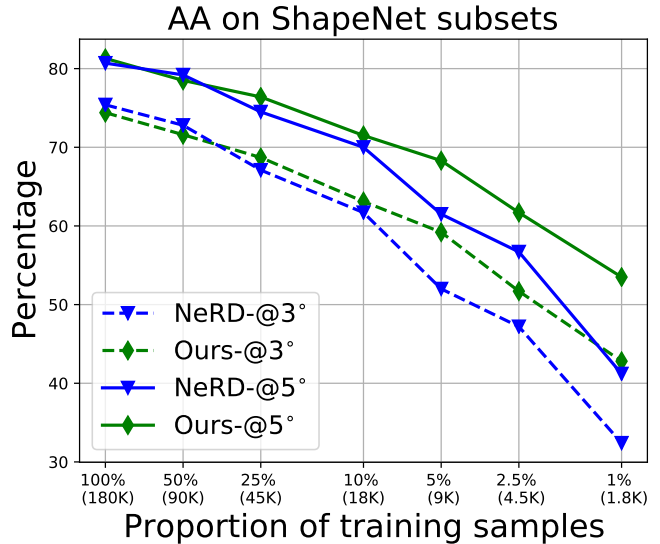


Figure 5: **Exp1: Data efficiency.** Comparison between NeRD and our model on various ShapeNet subsets. Both models are trained from scratch on each subset. The difference of the two models is insignificant when training data is ample (e.g., 10%). However, our model significantly outperforms NeRD on small subsets (e.g. less than 10K images), especially on 1% subset where the advantage is more than 10%.

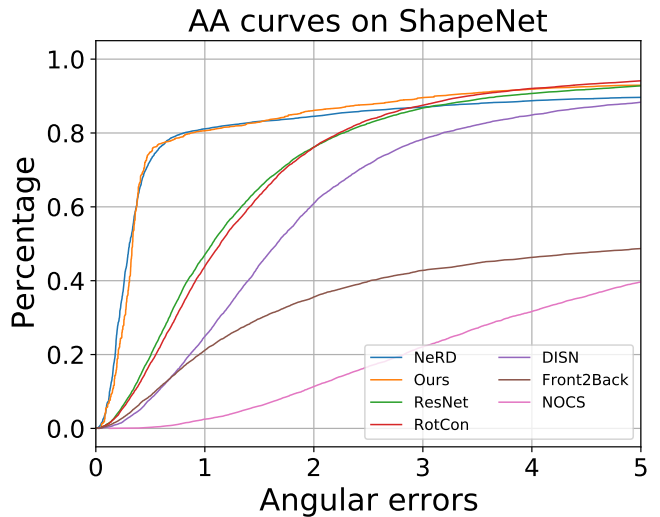


Figure 6: **Exp 2.1: Comparison on synthetic ShapeNet.** NeRD and our model shows substantial advantage over other models, particularly in low-error region.

performs the best but is approximately $\times 20$ slower than ours during inference (1.4 vs 25 frames per second). In comparison, the ResNet baseline using direct regression can only reach approximately 50% at 1° , indicating that naive

Datasets	ShapeNet[2]		
	AA@1°	AA@3°	AA@5°
ResNet [7]	20.8	55.7	69.5
RotCon [24]	18.7	54.6	69.4
DISN [22]	9.3	26.1	34.1
NOCS [19]	0.6	7.9	17.3
Front2Back [23]	9.3	26.1	34.1
NeRD [25]	57.3	75.4	80.7
<i>Ours</i>	55.7	75.5	82.0

Table 1: **Exp 2.1: Evaluation on synthetic ShapeNet.** Our model performs competitively on the synthetic ShapeNet dataset.

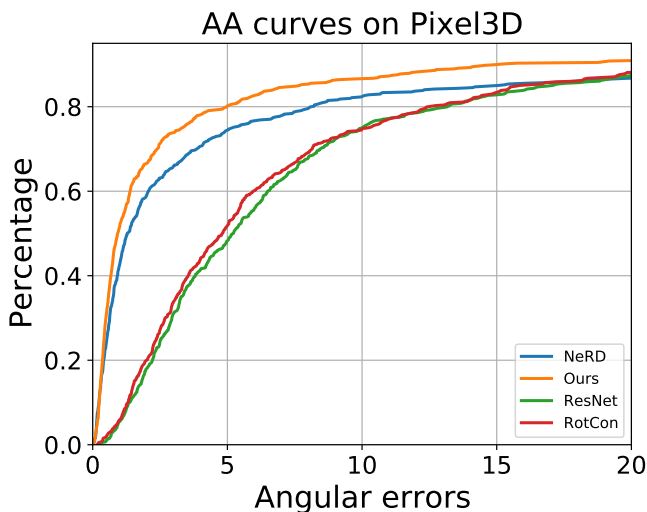


Figure 7: **Exp 2.2: Comparison on real-world Pixel3D dataset.** Our model performs the best on the challenging real-world dataset.

convolutions lack the ability to exploit the mirror symmetry, even though there is ample training data. We also notice that end-to-end approaches outperform these models relying on heavy post-processing, such as Front2Back.

4.3.2 Exp 2.2: Comparison on real-world data

To further validate the effectiveness of our model, we also test on the real-world Pixel3D dataset [18], as shown in Fig. 7 and Tab. 2. Our model outperforms all the other models consistently, thus demonstrating the superiority of our design. It is worth noting that the prediction error on Pixel3D is relatively larger than on ShapeNet. On one hand, there is limited training data (5,000 images in total), which is significantly less than ShapeNet. On the other hand, the camera configuration differs from image to image, thus

Datasets	Pixel3D[18]		
	AA@1°	AA@5°	AA@10°
ResNet [7]	1.5	12.3	23.6
Rotcon [24]	2.2	14.1	25.8
NeRD [25]	22.7	46.0	55.8
<i>Ours</i>	27.5	53.0	62.8

Table 2: **Exp 2.2: Evaluation on real Pixel3D dataset.** Our model performs the best on the real-world Pixel3D dataset.

	3D Mirror	Correlation volumes	Spherical convs	AA@1°	AA@5°
a	✗	✗	✗	0.8	9.5
b	✓	✓	✗	15.8	44.4
c	✓	✗	✓	8.0	31.5
d	✓	✓	✓	22.1	53.5

Table 3: **Exp 3: Ablation study.** We quantitatively verify the added value of 3D mirror geometry, 3D correlation volumes, and spherical convolutions.

making it hard to make precise prediction. Our model incorporates camera intrinsics into 3D mirror geometry, and therefore makes better prediction in different camera settings. Meanwhile, the usage of spherical convolutions contributes to the outstanding results on Pixel3D. NeRD lags behind due to a high demand for training data.

4.4. Exp 3: Ablation study

To verify the contribution of each component in our design, we conduct ablation studies, as shown in Tab. 3. All models are trained on the ShapeNet 1% subset. Model (a) is a simple baseline using direct regression and shows inferior results to the others in detecting 3D mirror geometry. We replace the spherical convolutions in our design (d) with 1×1 convolutions in model (b). Comparing (b) and (d), we find that spherical convolution improves the result significantly. In model (c), we replace the convolutions over the 3D cost volumes \mathcal{V} by taking the max over the depth dimension. By doing so, we only obtain the correspondence with highest correlation across different depth for each pixel, thus removing the 3D spatial information. However, model (c) underperforms substantially comparing to model (d), thus validating the necessity of 3D cost volumes. The ablation studies justify the added value of the 3D mirror, cost volumes and spherical convolutions

4.5. Discussion and limitation

Fig. 10 shows the impact of adding more training data from 1%, 10% to 100%. In the leftmost examples, our

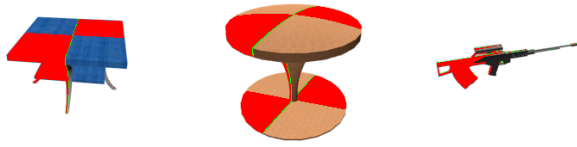


Figure 8: **Failure cases of our model on ShapeNet.** Our model fails in certain scenarios due to the presence of multiple symmetries and lacking correspondences. We highlight the ground truth in green and prediction errors in red.

model fails on the 1% subset, as it predicts the plane orthogonal to the ground truth. However, adding data helps the model to recover from the substantial mistake. The examples on the right show that adding data improves the overall precision qualitatively.

In Fig. 8, we show the failure cases of our model. The main challenge in these examples is that an object may admit multiple symmetries, thus leading to ambiguity. Moreover, it can be hard to find symmetric correspondences for certain objects, such as guns.

We also display results from the real-world Pixel3D dataset [18] in Fig. 11. In general, our model is able to detect the dominant mirror symmetry accurately from images unless multiple symmetries are present.

One major limitation is that we are only capable of predicting the global mirror plane. However, an object might admit multiple symmetries or local symmetries. Although we increase the inference speed by $\times 20$ over the top-performing model, there is still space for further speedup, since we calculate the correspondence for each pixel at all possible depth.

5. Conclusion

This paper studies 3D mirror symmetry detection from single-view perspective images, replying on well-founded geometric priors. We explicitly incorporate 3D mirror geometry into learning and propose multi-stage spherical convolutions to locate the optimal mirror plane precisely and efficiently. Our model is fully end-to-end trainable. Extensive experiments on both synthetic and real-world datasets shows the superiority of our model in both improved data efficiency and state-of-the-art performance. However, our model can only predict the primary mirror symmetry plane. Future work will focus on extending our model for detecting multiple types of symmetries, such as rotation symmetry and translation symmetry. Exploring the usage of 3D mirror in single-view 3D reconstruction, such as depth estimation and shape completion, would also be of interest.



Figure 9: **Qualitative results on ShapeNet when training on the 1% subset.** We compare the ground truth, predictions from NeRD and our results column by column. Both models are trained on the 1% subset only. The green line represents the projection of ground truth symmetry plane in images. The prediction errors between the prediction and ground truth planes are highlighted in red. In general, our model shows superior results over NeRD in small data regime.

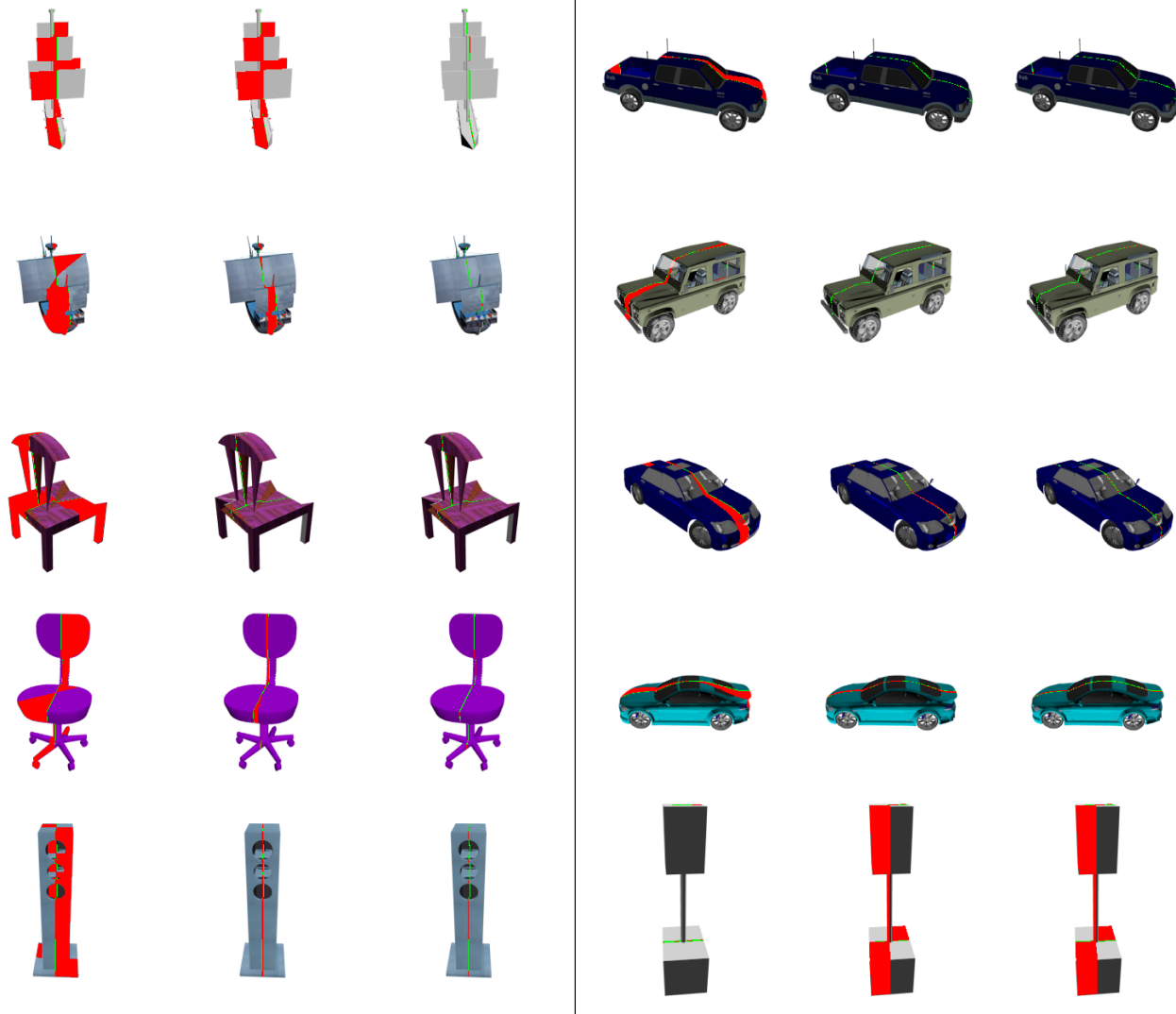


Figure 10: **Qualitative results on ShapeNet when adding more training data.** We compare the predictions from our models trained on the 1%, 10% and 100% (sub)sets. The green line indicates the ground truth symmetry axis. Adding more data helps the model to recover from making substantially wrong predictions, as shown on the left.



Figure 11: **Qualitative results on Pixel3D.** Our model is able to detect the dominant mirror symmetry from real-world images in most cases. However it fails to handle multiple symmetries (shown in the rightmost column). The ground truth symmetry axis is in green, while the prediction errors is highlighted in red.

References

- [1] David Cailliere, Florence Denis, Danielle Pele, and Atilla Baskurt. 3d mirror symmetry detection using hough transform. In *2008 15th IEEE International Conference on Image Processing*, pages 1772–1775. IEEE, 2008. 2, 3
- [2] Angel X Chang, Thomas Funkhouser, Leonidas Guibas, Pat Hanrahan, Qixing Huang, Zimo Li, Silvio Savarese, Manolis Savva, Shuran Song, Hao Su, et al. Shapenet: An information-rich 3d model repository. *arXiv preprint arXiv:1512.03012*, 2015. 1, 2, 4, 6
- [3] Christopher Funk, Seungkyu Lee, Martin R Oswald, Stavros Tsogkas, Wei Shen, Andrea Cohen, Sven Dickinson, and Yanxi Liu. 2017 iccv challenge: Detecting symmetry in the wild. In *Proceedings of the IEEE International Conference on Computer Vision Workshops*, pages 1692–1701, 2017. 2
- [4] Christopher Funk and Yanxi Liu. Beyond planar symmetry: Modeling human perception of reflection and rotation symmetries in the wild. In *Proceedings of the IEEE International Conference on Computer Vision*, pages 793–803, 2017. 2
- [5] L. Gao, L. X. Zhang, H. Y. Meng, Y. H. Ren, Y. K. Lai, and L. Kobbelt. Prs-net: Planar reflective symmetry detection net for 3d models. *IEEE Transactions on Visualization and Computer Graphics*, pages 1–1, 2020. 1, 2
- [6] Álvaro González. Measurement of areas on a sphere using fibonacci and latitude–longitude lattices. *Mathematical Geosciences*, 42(1):49–64, 2010. 4
- [7] Kaiming He, Xiangyu Zhang, Shaoqing Ren, and Jian Sun. Deep residual learning for image recognition. In *Proceedings of the IEEE conference on computer vision and pattern recognition*, pages 770–778, 2016. 5, 6
- [8] Sergey Ioffe and Christian Szegedy. Batch normalization: Accelerating deep network training by reducing internal covariate shift. In *International conference on machine learning*, pages 448–456. PMLR, 2015. 4
- [9] Diederik P Kingma and Jimmy Ba. Adam: A method for stochastic optimization. *arXiv preprint arXiv:1412.6980*, 2014. 5
- [10] Kevin Köser, Christopher Zach, and Marc Pollefeys. Dense 3d reconstruction of symmetric scenes from a single image. In *Joint Pattern Recognition Symposium*, pages 266–275. Springer, 2011. 1, 2, 3
- [11] Jingchen Liu, George Slota, Gang Zheng, Zhaohui Wu, Minwoo Park, Seungkyu Lee, Ingmar Rauschert, and Yanxi Liu. Symmetry detection from realworld images competition 2013: Summary and results. In *Proceedings of the IEEE Conference on Computer Vision and Pattern Recognition Workshops*, pages 200–205, 2013. 2
- [12] Minghua Liu, Lu Sheng, Sheng Yang, Jing Shao, and Shi-Min Hu. Morphing and sampling network for dense point cloud completion. In *Proceedings of the AAAI conference on artificial intelligence*, volume 34, pages 11596–11603, 2020. 1
- [13] Yi Ma, Stefano Soatto, Jana Kosecka, and S Shankar Sastry. *An invitation to 3-d vision: from images to geometric models*, volume 26. Springer Science & Business Media, 2012. 3
- [14] Adam Paszke, Sam Gross, Soumith Chintala, Gregory Chanan, Edward Yang, Zachary DeVito, Zeming Lin, Alban Desmaison, and A Antiga. L. and lerer. *Automatic differentiation in pytorch*, 2017. 4
- [15] Joshua Podolak, Philip Shilane, Aleksey Golovinskiy, Szymon Rusinkiewicz, and Thomas Funkhouser. A planar-reflective symmetry transform for 3d shapes. In *ACM SIGGRAPH 2006 Papers*, pages 549–559. 2006. 2
- [16] Konstantinos Sfikas, Theoharis Theoharis, and Ioannis Pratikakis. Rosy+: 3d object pose normalization based on pca and reflective object symmetry with application in 3d object retrieval. *International Journal of Computer Vision*, 91(3):262–279, 2011. 2
- [17] Yifei Shi, Junwen Huang, Hongjia Zhang, Xin Xu, Szymon Rusinkiewicz, and Kai Xu. Symmetrynet: Learning to predict reflectional and rotational symmetries of 3d shapes from single-view rgb-d images. *ACM Transactions on Graphics (SIGGRAPH Asia 2020)*, 39(6), 2020. 2
- [18] Xingyuan Sun, Jiajun Wu, Xiuming Zhang, Zhoutong Zhang, Chengkai Zhang, Tianfan Xue, Joshua B Tenenbaum, and William T Freeman. Pix3d: Dataset and methods for single-image 3d shape modeling. In *Proceedings of the IEEE Conference on Computer Vision and Pattern Recognition*, pages 2974–2983, 2018. 4, 6, 7
- [19] He Wang, Srinath Sridhar, Jingwei Huang, Julien Valentin, Shuran Song, and Leonidas J Guibas. Normalized object coordinate space for category-level 6d object pose and size estimation. In *Proceedings of the IEEE/CVF Conference on Computer Vision and Pattern Recognition*, pages 2642–2651, 2019. 5, 6
- [20] Yue Wang, Yongbin Sun, Ziwei Liu, Sanjay E Sarma, Michael M Bronstein, and Justin M Solomon. Dynamic graph cnn for learning on point clouds. *Acm Transactions On Graphics (tog)*, 38(5):1–12, 2019. 4
- [21] Shangzhe Wu, Christian Rupprecht, and Andrea Vedaldi. Unsupervised learning of probably symmetric deformable 3d objects from images in the wild. In *Proceedings of the IEEE/CVF Conference on Computer Vision and Pattern Recognition*, pages 1–10, 2020. 1
- [22] Qiangeng Xu, Weiyue Wang, Duygu Ceylan, Radomir Mech, and Ulrich Neumann. Disn: Deep implicit surface network for high-quality single-view 3d reconstruction. *arXiv preprint arXiv:1905.10711*, 2019. 1, 5, 6
- [23] Yuan Yao, Nico Schertler, Enrique Rosales, Helge Rhodin, Leonid Sigal, and Alla Sheffer. Front2back: Single view 3d shape reconstruction via front to back prediction. In *Proceedings of the IEEE/CVF Conference on Computer Vision and Pattern Recognition*, pages 531–540, 2020. 1, 5, 6
- [24] Yi Zhou, Connelly Barnes, Jingwan Lu, Jimei Yang, and Hao Li. On the continuity of rotation representations in neural networks. In *Proceedings of the IEEE/CVF Conference on Computer Vision and Pattern Recognition*, pages 5745–5753, 2019. 5, 6
- [25] Yichao Zhou, Shichen Liu, and Yi Ma. Nerd: Neural 3d reflection symmetry detector. In *Proceedings of the IEEE/CVF Conference on Computer Vision and Pattern Recognition*, pages 15940–15949, 2021. 1, 2, 3, 4, 5, 6